Astron. Astrophys. 358, 310–320 (2000)

ASTRONOMY AND ASTROPHYSICS

# Looking at the photon-dominated region in NGC 2024 through FIR line emission⋆

**T. Giannini[1,2,3], B. Nisini[1], D. Lorenzetti[1,3], A.M. Di Giorgio[3], L. Spinoglio[3], M. Benedettini[3], P. Saraceno[3], H.A. Smith[4], and G.J. White[5,6]**

[1] Osservatorio Astronomico di Roma, via Frascati 33, 00040 Monte Porzio, Italy
[2] Istituto Astronomico, Università La Sapienza, via Lancisi 29, 00161 Roma, Italy
[3] Istituto di Fisica Spazio Interplanetario – CNR Area Ricerca Tor Vergata, via Fosso del Cavaliere, 00133 Roma, Italy
[4] Harvard-Smithsonian Center of Astrophysics, 60 Garden Street, Cambridge, MA 02138, USA
[5] Queen Mary & Westfield College, University of London, Mile End Road, London E1 4NS, UK
[6] Stockholm Observatory, Saltsjöbaden, 13336, Sweden

Received 2 December 1999 / Accepted 27 March 2000

**Abstract.** We present the ISO-LWS spectra (45–200 $\mu$m) of both the molecular cloud NGC 2024 and its associated HII region. We observed the two Class 0 objects FIR3 and FIR5 and the infrared source IRS2. All the spectra appear quite similar, with approximately the same strength high-$J$ CO rotational lines (from $J_{\rm up}$=17 to $J_{\rm up}$=14), and atomic and ionic lines from oxygen, carbon and nitrogen. This uniformity suggests the bulk of the emission is from the extended cloud, and is not related to the local source conditions. The molecular emission has been modelled with a large velocity gradient (LVG) code, and the results imply that the emission originates in a clumpy, extended PDR with a temperature $T \sim 100$ K and a density $n_{\rm H_2} \sim 10^6$ cm$^{-3}$. CO column densities in excess of $10^{18}$ cm$^{-2}$ are derived for this molecular component. A line intensity ratio I([O I] 63 $\mu$m)/I([O I] 145 $\mu$m) of about 5 is found through all the region, indicating either that these two lines are both optically thick at the same temperature of CO, or, more likely, that the 63 $\mu$m line is strongly absorbed by cold foreground gas.

The ionised emission lines have been consistently modelled with CLOUDY; the lines arise from gas illuminated by an O9.5 star or its UV equivalent, representing the ionising capability of the whole OB cluster present in the region. From the intensity ratios of the ionic lines, relevant physical properties of the ionised gas (N/O abundance, electron density) are derived.

**Key words:** stars: formation – ISM: H II regions – ISM: individual objects: NGC 2024 – infrared: ISM: lines and bands

## 1. Introduction

The region NGC 2024 (Orion B, W12) is a well-studied, complex site of massive star formation, in which several different phenomena simultaneously occur. Located at a distance of 415 pc (Anthony-Twarog 1982), its complex morphology was disentangled by Thronson et al. (1984) and Barnes et al. (1989, hereinafter B89), who identified a dense molecular cloud within which an expanding HII region has been created by a bright, infrared cluster of young stars. They suggested that the HII region has broken the molecular cloud, and triggered massive star formation ahead of its ionisation front. Mezger et al. (1992) indeed found some protostellar condensations (from FIR1 to FIR7) just in front of the HII region, and subsequent investigations of these cores have revealed associated outflows and water maser emission (Sanders & Willner 1985, Richer 1990, Richer et al. 1992, Chandler & Carlstrom 1996). An estimate of the core mass has been obtained through sub-mm imaging (Visser et al. 1998). The kinetic temperature structure of the region has recently been investigated by Mangum et al. (1999), who found that some embedded condensations can be more evolved than isothermal protostars. Magnetic maps (Crutcher et al. 1999) indicate that the cloud is supported against collapse by non-thermal motions rather than static magnetic fields. A large scale view has been obtained by Graf et al. (1993, hereinafter G93) who performed a detailed multifrequency study of the molecular gas, deriving precise values for the temperatures and column densities of the major components. Their maps indicate that the warm gas is located close to the HII region, with a spatial distribution similar to the 1.3 mm dust continuum (Mezger et al. 1988).

This multifrequency analysis has been enriched by infrared observations performed in the last decade over all the NGC 2024 region. The [C II] 158 $\mu$m line has been mapped over a 35 by 45 arcmin area by Jaffe et al. (1994), while near infrared $H_2$ and [O I] 63 $\mu$m observations were carried out by Luhman et al. (1997). The far infrared emission, in particular, traces the gas cooling at intermediate conditions ($n_{\rm H_2} \sim 10^6$ cm$^{-3}$, $T \sim 10^2$ K). These values are representative of gas situated at the interface between the hot component (close to the central star) and the interstellar cold medium. This warm gas is exposed to the far-UV radiation from both the central star and the interstellar

*Send offprint requests to*: T.Giannini (teresa@coma.mporzio.astro.it)

⋆ Based on observations with ISO, an ESA project with instruments funded by ESA Member States and with the participation of ISAS and NASA

**Table 1.** Journal of observations

| Source | $\alpha$(1950.0) | | | $\delta$(1950.0) | | | Date | Orbit | $t_{\rm int}$ | $n_{\rm s}$ |
|---|---|---|---|---|---|---|---|---|---|---|
| | $h$ | $m$ | $s$ | $\circ$ | $'$ | $''$ | | | (sec) | |
| IRS2 | 05 | 39 | 14.3 | -01 | 55 | 54.7 | 10 Oct 1997 | 694 | 1.2 | 3 |
| FIR3 | 05 | 39 | 11.4 | -01 | 55 | 49.2 | 10 Oct 1997 | 694 | 4.8 | 12 |
| FIR5 | 05 | 39 | 12.7 | -01 | 57 | 03.3 | 10 Oct 1997 | 694 | 10 | 25 |
| OFF | 05 | 39 | 09.3 | -02 | 01 | 26.0 | 10 Oct 1997 | 694 | 4.8 | 12 |

field. Moreover, in most cases there is an additional interaction with the stellar wind, resulting in some heating by means of C or J shocks. According to model predictions (e.g. Draine et al. 1983, Hollenbach & McKee 1989), shocked gas cools mainly through the [O I], [C II], rotational $H_2O$ and high-$J$ CO lines, all of which fall in the spectral range (50–200 $\mu$m) covered by the Infrared Space Observatory (ISO).

In this paper the results of a spectroscopic study of NGC 2024 and its environment at far-IR wavelengths are presented. It is organised as follows: in Sect. 2 the observations and the data reduction procedures are described, while in Sect. 3 the results obtained from the analysis of line emission are reported. In Sect. 4 the origin of the molecular and atomic emission is discussed, along with the modelling of the ionic component. Finally our conclusions are summarised in Sect. 5.

## 2. Observations and data reduction

The NGC 2024 region was observed with the Long Wavelength Spectrometer (LWS: Clegg et al. 1996) on board the ISO satellite (Kessler et al. 1996). We performed four different pointings centred on IRS2, FIR3, FIR5 and one off-source position about 5′ south. The on-source targets are shown in Fig. 1 superimposed on the CO 7–6 and the 6 cm continuum maps taken by G93. Given the large LWS beam size ($\sim 80''$), there is some overlap of the beams, and in particular the FIR3 observation significantly overlaps with the IRS2 centred beam, and encompasses FIR2 and FIR4. The coordinates of the individual pointings are given in the journal of observations (Table 1, columns 2–7).

The spectra were obtained with the LWS AOT01 full grating scan mode (i.e. 43–197 $\mu$m wavelength range, resolution R $\sim$ 200, with the "fast scanning" option and an oversampling of 4 times the spectral resolution element). The integration time of each spectral sample ($t_{\rm int}$) and the number of spectral scans ($n_{\rm s}$) are given in columns 10 and 11 of Table 1 respectively. The raw data were reduced with the Off-Line Processing (OLP) version 7. The flux calibration was derived on the basis of Uranus observations (accuracy of about 30%, Swinyard et al. 1996) while the uncertainty in the wavelength calibration is about 25% of the resolution element (0.29 $\mu$m and 0.60 $\mu$m for the short (SW: 43–90 $\mu$m) and the long (LW: 90–197 $\mu$m) wavelength range respectively). Post-pipeline processing, including detector glitch removal, averaging of the different spectral scans, and interference fringes correction, was performed using the ISO Spectral Analysis Package (ISAP) version 1.6a.

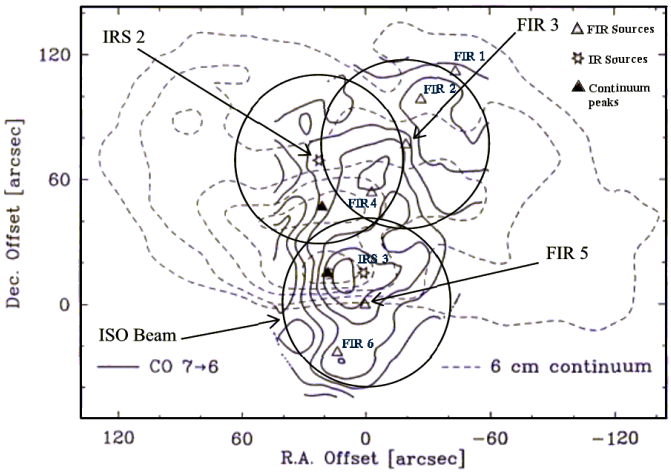


**Fig. 1.** ISO-LWS on-source targets superimposed on the CO 7–6 and 6 cm continuum maps adapted from G93. The (0,0) position indicates the source FIR5.

## 3. Results

The continuum subtracted spectra, obtained by means of first or second order polynomial fitting, are presented in Figs. 2 and 3 in the intervals where emission lines have been detected. All three on-source spectra appear quite similar: they all present strong atomic and ionic line emission. A weaker molecular component is detected via the high-$J$ CO pure rotational lines ($J_{\rm up}$ between 14 and 17), with the J=19–18 line also seen in the FIR3 and FIR5 spectra. In contrast with other Class 0 sources investigated with ISO (see e.g., Nisini et al. 1999, Benedettini et al. 2000), no trace of $H_2O$ emission is seen. In the off position there is no molecular emission; only the [O I] and [C II] lines are present, and these are about one order of magnitude weaker than on source. Thus, we did not subtract the off-source contribution from the on-source fluxes.

The adopted line detection criteria are: *i)* signal to noise ratio S/N $\gtrsim 3$; *ii)* difference between the fitted line centre and the vacuum wavelength compatible with the wavelength calibration uncertainty, *iii)* FWHM consistent within 20 % of the instrumental resolution element. The only exception to the *ii)* and *iii)* prescriptions is represented by the CO 17–16 line, whose FHWM is $\approx 1$ $\mu$m and $|\lambda_{\rm vac} - \lambda_{\rm obs}| > 0.3\,\mu m$ (see Sect. 3.1). In this case the line flux was calculated using a fixed width corresponding to the instrumental resolution. In Table 2 all the identified lines, as well as some relevant $3\sigma$ upper limits, are reported. The line shapes are quite well represented by gaus-

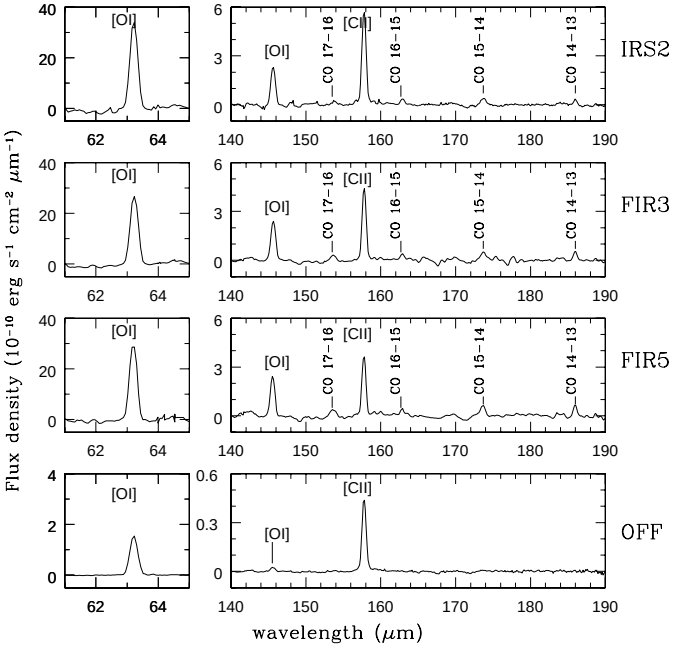


**Fig. 2.** Portions of the LWS continuum subtracted spectra of IRS2, FIR3, FIR5 and off position where [O I], [C II] and CO lines have been observed.

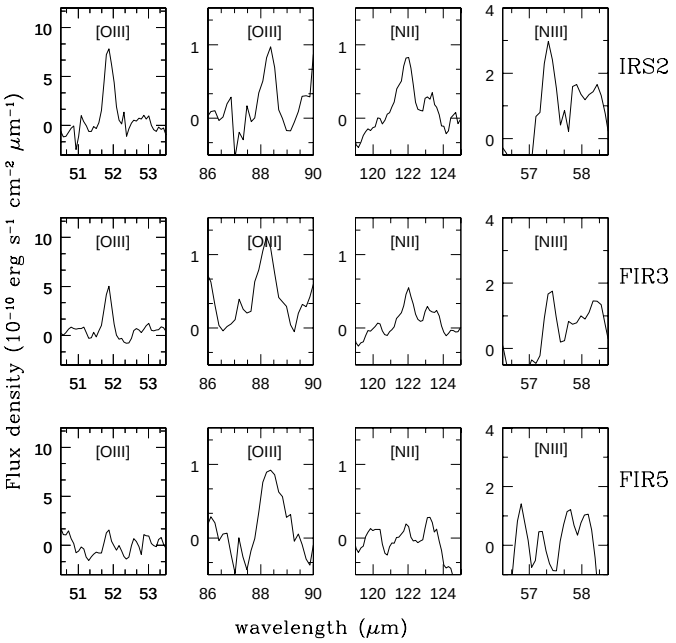


**Fig. 3.** As in Fig. 2 but for the ionic lines. In FIR5 the [N II] 122 $\mu$m and [N III] 57 $\mu$m lines are not detected but the spectrum is shown for comparison with the other sources.

sian profiles, which were fitted for deriving the integrated line fluxes. Given the high signal to noise ratio of the detected lines, the formal error from the fitting procedure results dominated by the rms fluctuations of the adjacent baseline, from which we estimated the relative $1\sigma$ statistical uncertainties.

From the inspection of Table 2 it is useful to compare, whenever is possible, the derived [C II] and [O I] 63 $\mu$m line intensities with the measurements performed in earlier works. In the [C II] map of the NGC 2024 region taken by Jaffe et al. (1994) the intensity peak, located nearby the peak of the HII region, has a value of 3.1 $10^{-3}$ erg s$^{-1}$ cm$^{-2}$ sr$^{-1}$. This position roughly corresponds to our pointing on IRS2 where we also find a maximum of the [C II] emission. If we assume beam filling, as reasonable given the diffuse nature of the emission, we find a peak brightness of 2.9 $10^{-3}$ erg s$^{-1}$ cm$^{-2}$ sr$^{-1}$, which is in agreement with that of Jaffe et al. The weaker emission they found south of DEC = -02°03′ ($\sim$ 2.5 $10^{-4}$ erg s$^{-1}$ cm$^{-2}$ sr$^{-1}$), is also comparable with the ISO observation in our OFF source position (2.0 $10^{-4}$ erg s$^{-1}$ cm$^{-2}$ sr$^{-1}$).

[O I] 63 $\mu$m line was previously observed at six positions centred on the continuum southern compact peak (SCP, Crutcher et al. 1986, see also Fig. 1) with a 22″ beam and a with 60″ offset in right ascension (Luhman et al. 1997 and references therein). Only the central position of this strip, in which the line intensity is 6.7 $10^{-3}$ erg s$^{-1}$ cm$^{-2}$ sr$^{-1}$, is encompassed by our observation centred on FIR5. Again assuming a unit filling factor, we obtain an intensity of 6.0 $10^{-3}$ erg s$^{-1}$ cm$^{-2}$ sr$^{-1}$, which is in agreement with the value by Luhman et al..

### *3.1. Additional features*

In addition to the emission lines reported in Table 2, the FIR3 and FIR5 spectra show several additional features that fulfill the above criteria for line detection. A careful inspection of the reduction procedures, however, indicates that these features cannot confidently be attributed to the source, but could arise in calibration when dividing the raw spectrum (photocurrent) with the Relative Spectral Response Function (RSRF), the response of the detectors as a function of wavelength as convolved with the theoretically corrected Uranus spectrum (Swinyard et al. 1996). The RSRF may contain several absorption features possibly due to Uranus itself but that are not accounted for by the theoretical model.

Roughly speaking these features become more and more apparent in sources with increasing continuum signal to noise. The effect can be evaluated more quantitatively by comparing the line to continuum ratio of the RSRF (L/C$_{\rm RSRF}$) and that of the corresponding spectrum feature (L/C$_{\rm spec}$). When L/C$_{\rm spec}$ $\lesssim$ L/C$_{\rm RSRF}$ the observed feature could be completely or partially contaminated by the RSRF. An example of each such an occurrence is shown in Fig. 4, where portions of the raw FIR5 spectrum (top panel), the RSRF (middle panel) and the FIR5 calibrated spectrum (bottom panel) are displayed. The vacuum wavelengths of CO and $H_2O$ lines are indicated in the bottom panel. It should be apparent (panel a) that the bulk of the features at the wavelengths of the higher-$J$ CO and water lines, whose L/C$_{\rm spec}$ $<$ L/C$_{\rm RSRF}$, are artificially introduced; in contrast, the CO 17–16 line (panel b) is real, and was clearly present in the photocurrent spectrum, although in the calibrated spectrum it has been broadened and shifted by the division. Because the integrated line fluxes have been artificially enhanced in this way, a more conservative method is to evaluate them by fixing the FWHM to the nominal value (0.60 $\mu$m), as we have done for

**Table 2.** Observed line intensities.

| Line Identification | $\lambda_{obs}$ ($\mu$m) | $\lambda_{vac}$ ($\mu$m) | F $\pm$ $\Delta$F ($10^{-11}$ erg s$^{-1}$ cm$^{-2}$) |
|---|---|---|---|
| *IRS2* | | | |
| [O III] $^3P_1 \rightarrow ^3P_2$ | 51.87 | 51.81 | 26 $\pm$ 4 |
| [N III] $^2P_{1/2} \rightarrow ^2P_{3/2}$ | 57.36 | 57.33 | 9$\pm$2 |
| [O I] $^3P_2 \rightarrow ^3P_1$ | 63.22 | 63.18 | 111$\pm$2 |
| [O III] $^3P_0 \rightarrow ^3P_1$ | 88.36 | 88.36 | 9$\pm$1 |
| [N II] $^3P_1 \rightarrow ^3P_2$ | 121.90 | 121.89 | 5.6$\pm$0.6 |
| CO 18$\rightarrow$17 | - | 144.71 | $<$1.5 |
| [O I] $^3P_1 \rightarrow ^3P_0$ | 145.58 | 145.52 | 21.3$\pm$0.5 |
| CO 17$\rightarrow$16 | 153.81$^\dagger$ | 153.27 | 1.5$\pm$0.2 |
| [C II] $^2P_{1/2} \rightarrow ^2P_{3/2}$ | 157.72 | 157.74 | 44$\pm$1 |
| CO 16$\rightarrow$15 | 162.92 | 162.81 | 1.8$\pm$0.2 |
| CO 15$\rightarrow$14 | 173.70 | 173.63 | 2.5$\pm$0.3 |
| CO 14$\rightarrow$13 | 185.95 | 186.00 | 2.2$\pm$0.3 |
| *FIR3* | | | |
| [O III] $^3P_1 \rightarrow ^3P_2$ | 51.87 | 51.81 | 15 $\pm$ 1 |
| [N III] $^2P_{1/2} \rightarrow ^2P_{3/2}$ | 57.40 | 57.33 | 5$\pm$1 |
| [O I] $^3P_2 \rightarrow ^3P_1$ | 63.23 | 63.18 | 83.0$\pm$0.6 |
| [O III] $^3P_0 \rightarrow ^3P_1$ | 88.42 | 88.36 | 6$\pm$1 |
| [N II] $^3P_1 \rightarrow ^3P_2$ | 122.02 | 121.89 | 3.6$\pm$0.8 |
| CO 20$\rightarrow$19 | - | 130.37 | $<$0.8 |
| CO 19$\rightarrow$18 | 137.09 | 137.20 | 0.9$\pm$0.3 |
| CO 18$\rightarrow$17 | - | 144.71 | $<$1.4 |
| [O I] $^3P_1 \rightarrow ^3P_0$ | 145.64 | 145.52 | 18.8$\pm$0.4 |
| CO 17$\rightarrow$16 | 153.63$^\dagger$ | 153.27 | 2.5$\pm$0.3 |
| [C II] $^2P_{1/2} \rightarrow ^2P_{3/2}$ | 157.78 | 157.74 | 29.1$\pm$0.2 |
| CO 16$\rightarrow$15 | 162.89 | 162.81 | 2.3$\pm$0.2 |
| CO 15$\rightarrow$14 | 173.65 | 173.63 | 3.4$\pm$0.4 |
| CO 14$\rightarrow$13 | 185.98 | 186.00 | 3.3$\pm$0.2 |
| *FIR5* | | | |
| [O III] $^3P_1 \rightarrow ^3P_2$ | 51.84 | 51.81 | 5 $\pm$ 1 |
| [N III] $^2P_{1/2} \rightarrow ^2P_{3/2}$ | - | 57.33 | $<$7.5 |
| [O I] $^3P_2 \rightarrow ^3P_1$ | 63.20 | 63.18 | 90$\pm$4 |
| [O III] $^3P_0 \rightarrow ^3P_1$ | 88.38 | 88.36 | 5$\pm$1.5 |
| [N II] $^3P_1 \rightarrow ^3P_2$ | - | 121.89 | $<$3.5 |
| CO 20$\rightarrow$19 | - | 130.37 | $<$0.6 |
| CO 19$\rightarrow$18 | 137.12 | 137.20 | 1.1$\pm$0.3 |
| CO 18$\rightarrow$17 | - | 144.71 | $<$1.4 |
| [O I] $^3P_1 \rightarrow ^3P_0$ | 145.55 | 145.52 | 17.7$\pm$0.4 |
| CO 17$\rightarrow$16 | 153.59$^\dagger$ | 153.27 | 3.1$\pm$0.3 |
| [C II] $^2P_{1/2} \rightarrow ^2P_{3/2}$ | 157.74 | 157.74 | 23.9$\pm$0.5 |
| CO 16$\rightarrow$15 | 162.94 | 162.81 | 3.0$\pm$0.3 |
| CO 15$\rightarrow$14 | 173.62 | 173.63 | 5.0$\pm$0.3 |
| CO 14$\rightarrow$13 | 185.97 | 186.00 | 4.8$\pm$0.4 |
| *OFF* | | | |
| [O I] $^3P_2 \rightarrow ^3P_1$ | 63.18 | 63.18 | 5$\pm$1 |
| [O I] $^3P_1 \rightarrow ^3P_0$ | 145.57 | 145.52 | 0.19$\pm$0.02 |
| [C II] $^2P_{1/2} \rightarrow ^2P_{3/2}$ | 157.78 | 157.74 | 3.1$\pm$0.3 |

$^\dagger$ difference between $\lambda_{obs}$ and $\lambda_{vac}$ not compatible with the wavelength calibration uncertainty and FHWM broader than 20% of the instrumental resolution element (see text).

**Table 3.** Additional features.

| RSRF feature ($\mu$m) | LWS Detector | Possible (Mis)-Identification | $\lambda_{vac}$ ($\mu$m) |
|---|---|---|---|
| 72.71 | SW4 | CO 36–35 | 72.84 |
| 75.39 | SW4 | o$H_2O$ $3_{21}$-$2_{12}$ | 75.38 |
| 77.04 | SW4 | CO 34–33 | 77.06 |
| 111.99 | LW2 | HD | 112.08 |
| 141.14 | LW3 | $CO^+$ 18–17 | 141.48 |
| 149.69 | LW3 | $CO^+$ 17–16 | 149.76 |
| 151.24 | LW4 | $^{13}$CO 18–17 | 151.43 |
| 153.59 | LW4 | CO 17–16 | 153.27 |
| 159.16 | LW4 | $CO^+$ 16–15 | 159.10 |
| 159.85 | LW4 | $^{13}$CO 17–16 | 160.30 |

deriving the CO 17–16 fluxes reported in Table 2. In Table 3 we list the vacuum wavelengths (column 1) of the emission features we have detected in the FIR3 and FIR5 spectra at S/N $\gtrsim$ 3 and that could be strongly contaminated by the RSRF spectrum. All the listed features lie close to typical molecular transitions, which span the (45–200 $\mu$m range), emitted in star forming enviroments (columns 3 and 4). Among them, the feature at 111.99 $\mu$m as been already recognised as a spurious line (see e.g. Wright et al. 1999). The averaged L/$C_{RSRF}$ ratio is 0.02: this value can be compared with the measured L/$C_{spec}$ in order to give a rough estimate of the reliability of the line detection; we remark however that this tricky matter deserves a more detailed treatment which is beyond the aims of the present paper.

## 4. Analysis and discussion

### *4.1. Description of the encompassed region*

The LWS observations cover an area which encompasses both the dense cores with the embedded FIR sources, and the HII region associated with the OB cluster. The schematic diagram of the region presented in Fig. 5, adapted from B89, gives a clearer view of all the components along the line of sight. As viewed from the west, three different physical situations appear: a cold gas component (T$\sim$ 25 K, G93) with a high optical depth, an HII region where the OB star association (including IRS2 and IRS3) is located and finally a dense molecular cloud with the embedded FIR sources. As pointed out by G93, the physical connection between the molecular and the ionised gas is clearly indicated by the CO 7–6 contour map, whose peaks coincide with the 6 cm continuum emission coming from the HII region. Because of its high optical depth, the 7–6 line is a tracer of the temperature distribution of the molecular ridge surface, and thus the shape of the contour levels is determined by the same heating sources responsible for the continuum emission, suggesting that the molecular ridge is very close to the interface with the HII region (G93, see also Fig. 1).

The molecular gas has been probed not only with the 7–6 CO line, but also through multiline maps of the CO isotopes ($^{13}$CO, $C^{17}O$, $C^{18}O$) at millimeter and submillimeter wavelengths (Graf et al. 1990, hereinafter G90, G93). All the mapped lines are quite narrow ($\Delta v_{LSR} \sim 2$ km s$^{-1}$), indicating that they are emitted

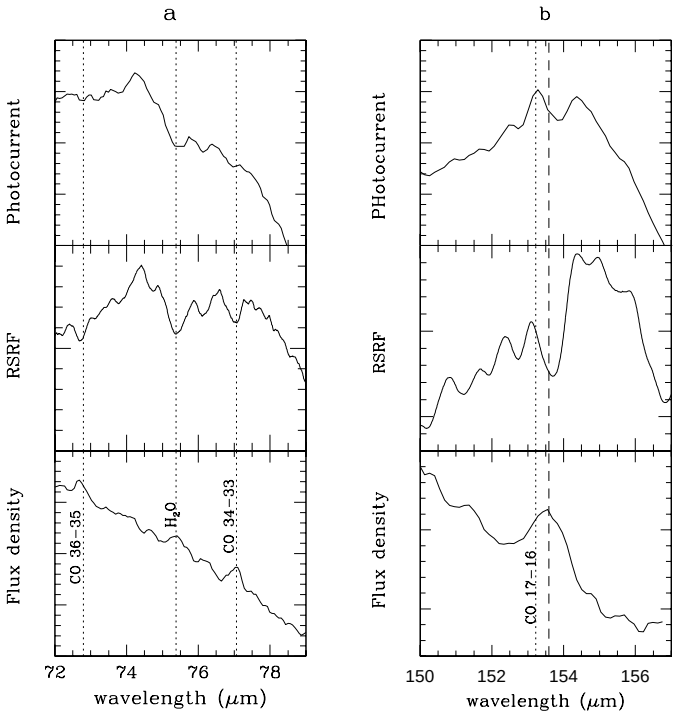


**Fig. 4. a** FIR5 photocurrent spectrum (top panel), Relative Spectral Response Function (middle panel) and Flux density (bottom panel) in the wavelength range 72–79 $\mu$m (arbitrary units). The dotted lines indicate the vacuum wavelengths of some CO and $H_2O$ lines. **b** As in **a**, but in the wavelength range 150–157 $\mu$m. The dashed line indicates the fitted central wavelength of the CO 17–16 line.

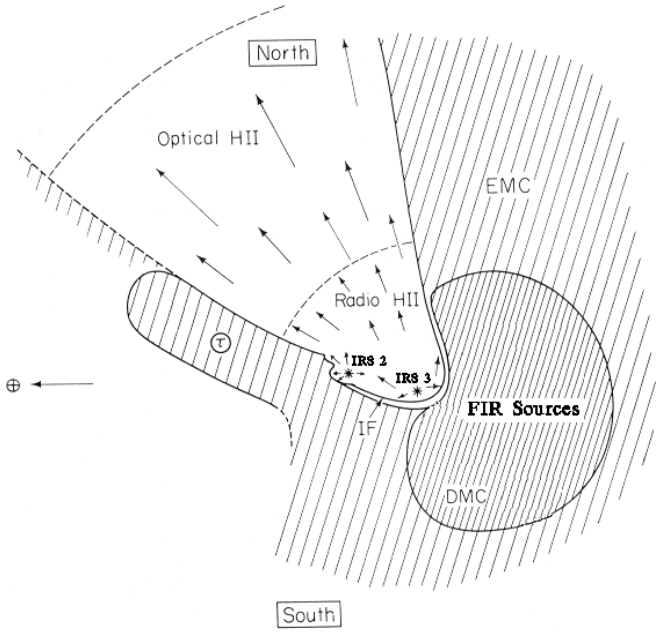


**Fig. 5.** Schematic view projected from the west of the NGC 2024 region. Abbreviations are as follows: EMC = extended molecular cloud, DMC = dense molecular cloud, IF = ionisation front, $\tau$ = high optical depth cloud. Adapted from B89.

from quiescent gas and that the origin of the molecular heating is probably the far ultraviolet (FUV) component of the radiation field associated with the nearby OB star cluster.

### *4.2. The CO emission lines*

We first investigated the physical conditions of the medium where the high-$J$ CO lines originate. Assuming this gas is the same as that responsible for the 7–6 transition, we fitted the observed line flux distribution using physical conditions similar to those found by G93 (that is, temperatures of the order of 100 K, and a density $\sim 10^6$ cm$^{-3}$). We used a large velocity gradient code in a plane parallel geometry, taking into account the first 23 CO rotational levels. The collisional downward rates by impacts of $H_2$ molecules for each pair of levels with $J_{\rm up} \leq 22$ and $10 \leq T \leq 250$ K are computed from the $\gamma_{J0}$ coefficients, which represent the de-excitation rates from a level $J$ to the ground level 0, taken from Flower & Launay (1985). Upward rates were computed using the principle of detailed balance. Radiative decay rates were taken from Chackerian & Tipping (1983).

The free parameters of our model are: gas kinetic temperature, density and ratio between column density and intrinsic linewidth. Together with the filling factor, which depends only on the absolute line intensities, these have been constrained to precise values, because the observed fluxes have small associated uncertainties and effectively trace the peak of the CO emission as a function of $J_{\rm up}$. Further constrains on the parameters are given by the low-$J$ lines observations carried out by G93. The 7–6 line flux was derived from their $\sim 3' \times 3'$ map covering the LWS beams centred on FIR3 and FIR5, while the CO 3–2 and 6–5 were observed with a $8''$ beam toward FIR5. Since the low-$J$ emission appears diffuse and at approximately the same intensity level, the total flux was derived by integrating over the whole LWS beam and then compared with our model's predictions. The associated errors were assumed equal to the calibration uncertainty (30%).

The fitting procedure we used was first to fix the intrinsic linewidth at 2 km s$^{-1}$, (the FWHM of the background gas component, G93), and then to use the observed line flux distribution as a function of $J_{\rm up}$ to derive the gas temperature ($T$) and density ($n_{\rm H_2}$), and to define the optical depth of the lines. In Fig. 6 the obtained fits are reported. For each source the two curves correspond to the extreme values of $T$ and $n_{\rm H_2}$. We note that the CO 16–15 line in FIR3 and FIR5 is systematically lower than the obtained fits. We have investigated possible instrumental reasons related to contamination by spurious features, fringing effects, similar occurrence in other spectra, all with negative results. Hence at the moment we remain with no plausible explanation for that.

The good agreement with the low-$J$ line fluxes indicates that a self-consistent picture of the CO emission can be made with only one component. The derived temperature and density are roughly equal ($100 \lesssim T \lesssim 200$ K and $5\ 10^5 \lesssim n_{\rm H_2} \lesssim 2\ 10^6$ cm$^{-3}$) at all the positions we sampled, and are comparable with the values found by G90 and G93. The full set of the derived parameters is listed in Table 4, with both the low and high tem-

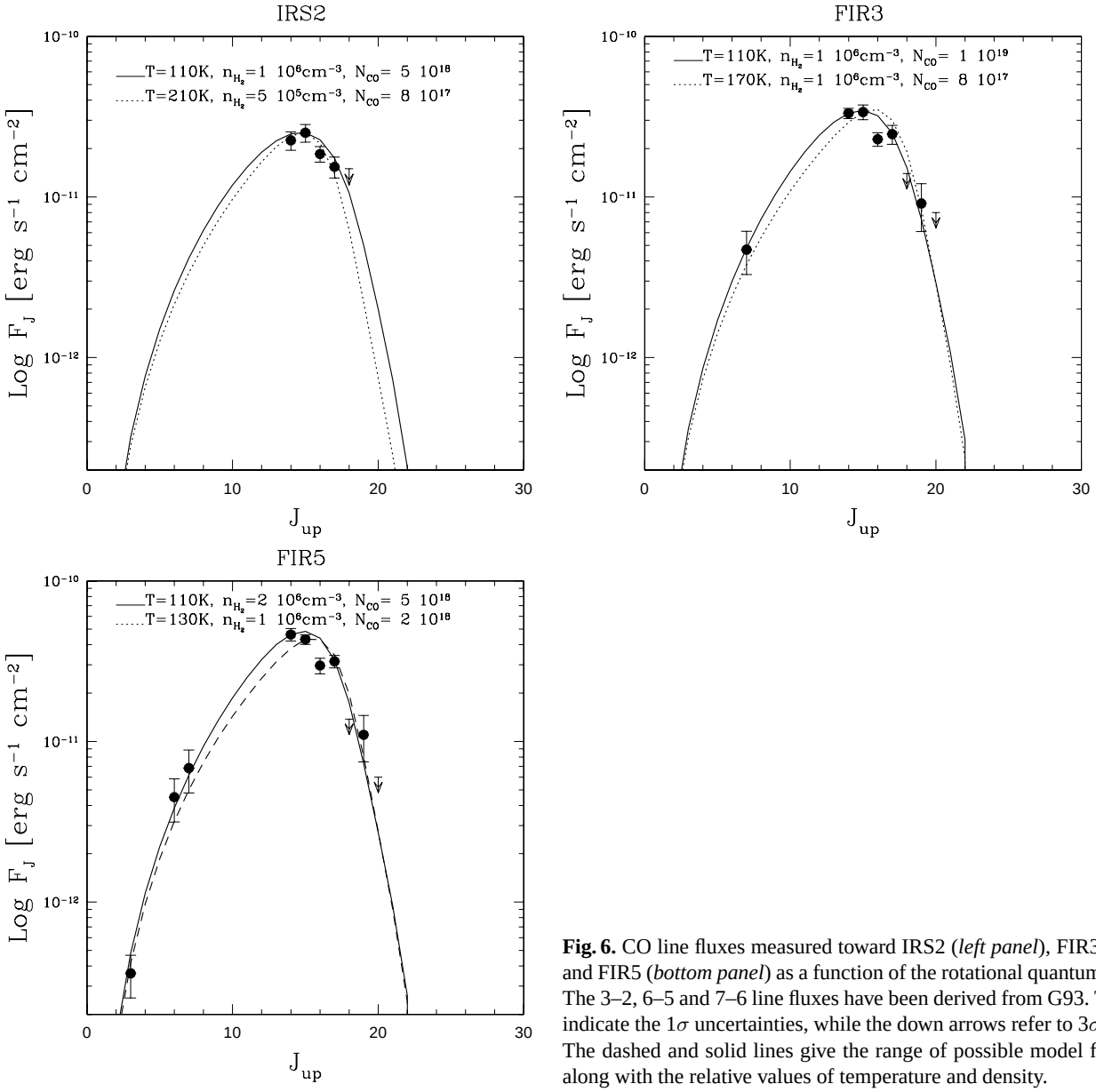


**Fig. 6.** CO line fluxes measured toward IRS2 (*left panel*), FIR3 (*right panel*) and FIR5 (*bottom panel*) as a function of the rotational quantum number $J_{\rm up}$. The 3–2, 6–5 and 7–6 line fluxes have been derived from G93. The error bars indicate the $1\sigma$ uncertainties, while the down arrows refer to $3\sigma$ upper limits. The dashed and solid lines give the range of possible model fits to the data along with the relative values of temperature and density.

perature cases shown. The model predicts the 7–6 line should be optically very thick everywhere ($\tau > 10$), in agreement with the observational findings of G93, and unlike the high-$J$ CO lines whose optical depths are of the order of unity. This difference allows us to use the high-$J$ lines for deriving the CO column density $N$(CO) of the emitting region. Indeed the intensity ratio between two lines which are not fully thermalised is a very sensitive function of the column density in the range where they become optically thick (Nisini et al. 1999). As an example, Fig. 7 shows the intensity ratio I(CO 17–16)/I(CO 14–13) as a function of $N$(CO), at $T$=100 K and n=$10^6$ cm$^{-3}$. The ratio is very sensitive to $N$(CO) in the range $10^{18}$ - $10^{21}$ cm$^{-2}$. The hatched area represents the measured line ratio for the FIR3 spectrum. Applying a similar procedure to all of the observed ratios, we derive $N$(CO) values over the whole region ranging between 8 $10^{17}$ - 1 $10^{19}$ cm$^{-2}$, implying $N$(H$_2$) values of 8 $10^{21}$ - 1 $10^{23}$ cm$^{-2}$ assuming the CO abundance $X$(CO) = $10^{-4}$. The higher value is in good agreement with the determinations obtained from large beam observations (Mundy et al. 1987, Snell et al. 1984), but remains below the measurements on the density peaks (G90, Schultz et al. 1991, Moore et al. 1989).

The angular dimension of the emitting region can be derived from the ratio between the absolute line fluxes and the CO column density. We have found that for each pointed position the emission fills the LWS beam, thus the spatial extent of the higher-$J$ CO emission covers an area of at least $2' \times 2.6'$, comparable to that mapped by G93 in the 7–6 line. At the adopted distance of 415 pc the angular dimension corresponds to $\sim$ 0.32 pc, or about twenty times larger than the depth estimated from the column-to-volume density ratio (typically 5 $10^{22}/10^6$ cm = 0.016 pc). This result strongly supports the hypothesis that the warm gas is clumpy. This is actually expected,

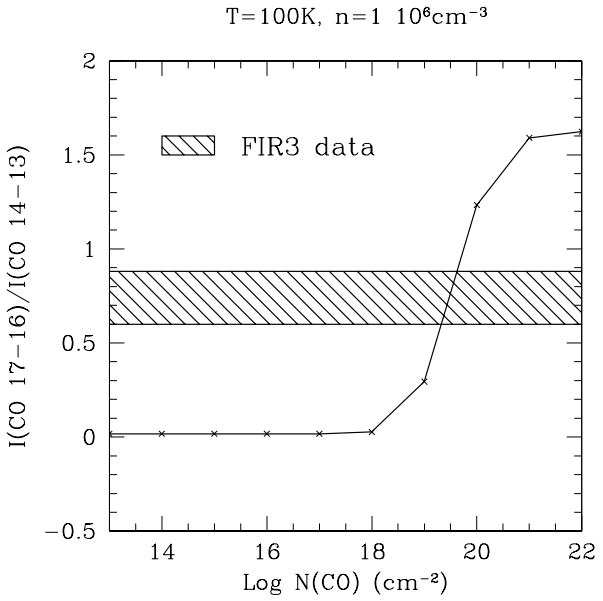


**Fig. 7.** Intensity ratio I(CO 17–16)/I(CO 14–13) vs. $N$(CO) computed at $T$=100 K and $n$=$10^6$ cm$^{-3}$. The FIR3 observed ratio is shown as an hatched area.

since high column densities of warm CO in the FUV illuminated interface region can be present only in clumpy media, where self shielding of molecules can shrink the FUV absorption layer and move it up towards the exciting sources. Thus our findings extend to the NGC 2024 region similar results obtained through CO observations towards quiescent, FUV-heated regions (e.g. Harris et al. 1987, Stutzki et al. 1988, Jaffe et al. 1990, Giannini et al. 1999).

### *4.3. The [O I] and [C II] lines*

Having now determined the physical conditions of the CO gas we next try to model the [O I] and [C II] emission as coming from the same PDR region as the CO lines. We first note (see Table 5, column 2) that the I([O I]63)/I([O I]145) line ratios are fairly similar for the three on-source positions, amounting to $\sim$ 5, while the off-source ratio is definitively enhanced. [O I] line ratios lower than 10 are never predicted in PDRs unless both lines are optically thick and the temperature is less than 500 K (e.g. Tielens & Hollenbach 1985, their Fig. 2). In such cases the ratio is given by the Planck function values at the lines wavelengths, and so depends only on the temperature. The blackbody ratios at the temperatures derived from the CO fits and for lines with the same widths are given in Table 5 (column 3). The computed values agree well with the observed ratios, with the possible exception of FIR3. Moreover, also the absolute brightness of the two lines is consistent with the blackbody emission at T$\sim$ 100 K, assuming complete beam filling and $\Delta$v = 2 km s$^{-1}$. At the temperatures derived from the CO lines and assuming that all oxygen is in the O$^o$ form, with an abundance $X$(O) = 3.2 $10^{-4}$ (Meyer et al. 1998), we derive that $N$(H) $\sim$ $10^{21}$ cm$^{-2}$ and $N$(H) $\sim$ 2 $10^{22}$ cm$^{-2}$ are needed in order to have $\tau$=1 for the 63 $\mu$m and 145 $\mu$m [O I] lines, respectively. These $N$(H) values are consistent with those derived from the CO fits, thus we could reasonably affirm that both the [O I] lines come from the same gas as the CO emission lines. Nevertheless, this conclusion cannot be easily reconciled with the scenario described in Sect. 4.1 and illustrated in Fig. 5: we are observing through regions with different ionisation levels and temperatures, and hence it is unreasonable to think that the [O I] emission originates only in the background cold gas of the dense core. Indeed PDR models (see e.g. Hollenbach & Tielens 1997, Kaufman et al. 1999) predict the bulk of the cooling and the strongest [O I] emission flux is at $T\geq$500 K, and at lower temperatures the molecular emission dominates the gas cooling, so that the observed [O I] line emission can indeed come from the interface between the HII region and the extended PDR. However in this case the lines would be both optically thin and their expected intensity ratio $\geq$ 10. The contrasting observational proof can be explained with the absorption of the [O I] 63 $\mu$m line from the foreground cold gas present along the line of sight (see Fig. 5). This hypothesis is strenghtened by ISO observations toward the enviroments of high mass YSOs and PMS stars (Saraceno et al. 1998, Lorenzetti et al. 1999). Moreover, [O I] 63 $\mu$m in absorption has been directly observed by high resolution KAO observations in regions similar to NGC 2024 (Poglitsch et al. 1996, Kraemer et al. 1998).

We next started by investigating the origin of the [C II] 158 $\mu$m emission. From its absolute brightness an excitation temperature of $\sim$ 300 K can be derived again assuming beam filling and $\Delta$v = 2 km s$^{-1}$. Since the excitation temperature represents the minimum kinetic temperature for the emitting gas, we can rule out the possibility that the line is emitted by the 100 K gas and, on the contrary, this occurrence suggests that it mainly comes from the warmer part of the PDR. This result is in general agreement with the findings of Jaffe et al. (1994), who indicate the clumps surfaces as the favoured sites of the emission. Additional contributions to the total $C^+$ emission could arise from the ionised gas. This possibility has been investigated by Heiles (1994) and by Petuchoskwi & Bennett (1993), who showed that in the classical HII regions the [C II] 158 $\mu$m line intensity ranges between 1 and 20 times the [N II] 122 $\mu$m line intensity. As we will show in Sect. 4.5 and in Table 7, however, the ionised gas contributes only about 10% to the total $C^+$ flux, except in the case of FIR5 where it contributes 30% of the measured value.

Finally, the detection of both O$^o$ and $C^+$ in the off source position suggests the presence of a faint, diffuse atomic emission component over larger dimensions, as also probed by the observations by Jaffe et al. (1994). The intensity ratio between the [O I] and [C II] lines is in agreement with the predictions for diffuse PDR models (Kaufman et al. 1999). For the off position a density of $\sim$ 5 $10^4$ cm$^{-3}$ and a field flux of $10^3$ $G_o$, (being $G_o$ = 1.6 $10^{-3}$ erg s$^{-1}$ cm$^{-2}$, Habing 1968), are derived.

### *4.4. The PDR parameters*

Having established the consistency of a model in which both the atomic and molecular emission arise in a common, photon-

**Table 4.** Physical parameters of the CO emission.

| | IRS2 | FIR3 | FIR5 |
|---|---|---|---|
| Gas temperature $T$(K) | 110–210 | 110–170 | 110–130 |
| Gas density $n_{\rm H_2}$ (cm$^{-3}$) | $1 \cdot 10^6$ - $5 \cdot 10^5$ | $1 \cdot 10^6$ | $2 \cdot 10^6$ - $1 \cdot 10^6$ |
| CO column density $N_{\rm CO}$ (cm$^{-2}$) | $5 \cdot 10^{18}$ - $8 \cdot 10^{17}$ | $1 \cdot 10^{19}$ - $8 \cdot 10^{17}$ | $5 \cdot 10^{18}$ - $2 \cdot 10^{18}$ |
| CO cooling $L$(CO) ($L_\odot$) | 0.9–1.0 | 1.2–1.3 | 1.5–1.8 |

**Table 5.** I([O I]63)/I([O I]145)

| Source | Observations | Blackbody† |
|---|---|---|
| IRS2 | $5.2 \pm 0.2$ | 5.9–8.5 |
| FIR3 | $4.4 \pm 0.1$ | 5.9–7.8 |
| FIR5 | $5.1 \pm 1.3$ | 5.9–6.4 |
| OFF | $26 \pm 8$ | - |

† The reported ratios refer to the temperatures derived from the CO line flux distribution fits.

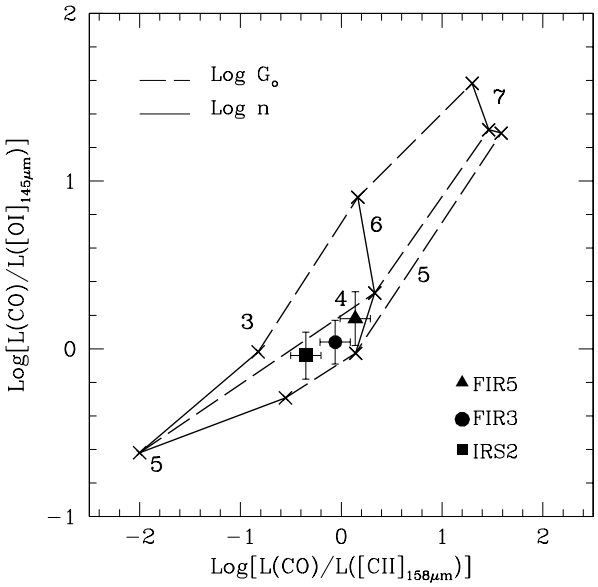


**Fig. 8.** Observed luminosity ratios $L$(CO)/$L$([O I]145) vs. $L$(CO)/$L$([C II]158) superimposed on clumpy PDR models by Burton et al. (1990) for different values of $n$ and $G_{\rm o}$.

dominated region, we want now to derive the physical parameters of the PDR. For this purpose we will refer to the prediction of the clumpy PDR model by Burton et al. (1990). Although the [O I] 63 $\mu$m line is one of the main coolants in photon-dominated regimes, we did not consider this line in our analysis because, as noted above, it could be strongly absorbed. Instead, we have exploited the luminosity ratios $L$(CO)/$L$([O I]145) and $L$(CO)/$L$([C II]158), which are plotted in Fig. 8 superimposed on a grid with different values of $G_{\rm o}$ and $n$. We assumed all the [C II] 158 $\mu$m line originated in the PDR region since the subtraction of the contribution due to the ionised gas does not significantly change the observational points inside the grid. The uncertainties on the [O I] and [C II] luminosities were derived from the measured fluxes, while the error associated with $L$(CO) was taken as the mean deviation between the two determinations derived from the LVG fits (see Table 4).

The derived densities are, for all the sources, somewhere between $5\ 10^5$ and $10^6$ cm$^{-3}$, in agreement with those derived from the CO fits, while the intensity field is $\sim 5\ 10^4\ G_{\rm o}$ everywhere.

This value can be compared with the $G_{\rm o}$ produced by the OB star cluster to derive the depth of the FIR sources inside the core. To account for the measured radio flux the whole cluster has been represented by an equivalent O9.5 ZAMS star (B89). To a first approximation we can locate this equivalent star at the IRS2 position, because this source has the earliest spectral type in the cluster (B0.5 ZAMS star; Thompson et al. 1981; Jiang et al. 1984), and underwent a large outburst at the end of the last decade, providing enough photons to substain the whole ionisation (Nisini et al. 1994). Even were the field intensity unaffected by the extinction, the estimated $G_{\rm o}$ value would be reached at a distance of only 0.2 pc from IRS2 – comparable with the linear distance from FIR3 (0.09 pc) and FIR5 (0.15 pc). This indicates that the FIR sources are indeed very close to the interface between the dense core and the HII region, thus confirming what is suggested by the comparison between the CO 7–6 and the 6 cm continuum maps, and strongly favouring a scenario in which the star formation in the molecular core is triggered by the expanding ionised gas. Moreover, the high $G_{\rm o}$ value explains the absence of water emission from the FIR sources: even though water is expected to be among the main coolants in the enviroment around energetic outflows, it can be easily destroyed by a strong FUV field, which may still permeate the gas.

### *4.5. The photoionised emission*

#### 4.5.1. The electron density and CLOUDY predictions

The emission from the HII region is traced by the nitrogen and oxygen ionic lines we detected in all three on-source pointings. In order to infer the physical properties of the ionised region, we fitted the observed line luminosities with the photoionisation code CLOUDY (version C90.05, Ferland 1996). Because CLOUDY's predictions depend on several input parameters, we first used the observed intensity ratios to constrain independently the electron density ($N_{\rm e}$) in each observed region. The ionic forbidden line transitions from levels with $\Delta J$=1 are a useful tool for doing this (e.g., Rubin et al. 1994, hereinafter R94), inasmuch as, compared to the optical or near infrared lines, they are relatively insensitive to the extinction and depend only slightly on the electron temperature. Moreover, because the ion-

**Table 6.** Ionic lines ratios and derived electron densities

| Source | I([O III]52)/I([O III]88) | I([N III]57)/I([N II]122) | $N_e$ [O III] ($cm^{-3}$) | $N_e$ [N II] ($cm^{-3}$) |
|---|---|---|---|---|
| IRS2 | $2.9 \pm 0.7$ | $1.6 \pm 0.5$ | 1500 | 6000 |
| FIR3 | $2.5 \pm 0.6$ | $1.1 \pm 0.5$ | 1200 | 2500 |
| FIR5 | $1.9 \pm 0.5$ | - | 100 | - |

isation equilibrium predicts a stratification of different species with increasing distance from the central star, the simultaneous detection of lines from different ions allows more than one determination of $N_e$ and then an evaluation of the density gradient throughout the HII region. Following the model of R94, we can directly evaluate $N_e$ from the I([O III]52)/I([O III]88) ratio, which probes the density in the range $10^2 - 10^5$ cm$^{-3}$. The $N_e$[O III] estimates are reported in Table 6 (column 4): they are of the order of $\sim 10^3$ cm$^{-3}$ in IRS2 and FIR3 and $10^2$ cm$^{-3}$ in FIR5, probably because this pointing covers the external edge of the HII region closeby the molecular gas (see Fig. 1). This electron density (which could, in a first approximation, also be attributed to the region emitting the [N III] line), might substantially differ from that derivable from the [N II] emission ($N_e$[N II]). We can not provide directly $N_e$[N II], which is generally derived by the ratio I([N II]205)/I([N II]122), because the [N II] 205 $\mu$m line is just outside of the wavelength range covered by LWS. However, following the method developed in R94, an indirect estimate of $N_e$[N II] can be obtained from the fractional ionisation derivable from the 57 $\mu$m and 122 $\mu$m lines. This is given by:

$$\frac{\langle N^{++}\rangle}{\langle N^{+}\rangle} = \frac{F_{57}/\epsilon_{57}}{F_{122}/\epsilon_{122}} \quad (1)$$

where $\epsilon_\lambda$ = j$_\lambda$/($N_e$N$_i$), j$_\lambda$ being the volume emissivity for the line and N$_i$ the ion density. In this formula $\epsilon_{122}$ (that depends on $N_e$[N II]) has to be considered as an unknown quantity. Indeed $\langle$N$^{++}\rangle/\langle$N$^{+}\rangle$ is a function of the spectral type of the ionising star, and can be evaluated from the relationship with the effective temperature (R94, their Fig. 4). Given the $N_e$[N III] values derived before, $\epsilon_{57}$ can be estimated from R94 (their Fig. 3), which is also used, once $\epsilon_{122}$ is computed from (1) to derive $N_e$[N II]. This latter one is shown in column 5 of Table 6. For both IRS2 and FIR5 it increases slightly faster than $N_e$[O III] does, indicating that the density slowly increases going away from the bulk of the HII region toward the background molecular core.

Presuming this density enhancement is not dramatic, we have taken the electron density as equal to the estimated $N_e$ [O III] in our CLOUDY modelling. We have fixed the spectral type of the photoionising star as O9.5, and adjusted both the extinction hydrogen column density and the distance from the cluster in order to reproduce the observed luminosities. The best fits were obtained for $N$(H) $\sim 10^{18}$ cm$^{-2}$, and for distances between 0.1 and 0.2 pc. The general agreement between the observed and estimated luminosities (see Table 7) confirms independently what we previously derived from the molecular analysis. In particular it confirms the assumption about the ionising capability of the star cluster and the small distance between the HII region and the dense core. The [O III] luminosities are better modelled everywhere. The [N II] and [N III] luminosities result alternatively in having under/over estimated values, possibly because of the density gradients occurring over the HII region. The [C II] 158 $\mu$m line from the ionised gas is only a small fraction of the observed flux, testifying to the fact that the bulk of the emission is due to the photodissociated gas as we have already anticipated in Sect. 4.3. Finally, as expected, the contribution of both the [O I] lines is negligible.

#### 4.5.2. The N/O abundance

The [N III] and [O III] lines enable us to measure the N/O abundance in the HII region. It is well known that abundance estimates derived from FIR lines result generally in significantly higher values than those obtained from the $N^+/O^+$ ratio using optical lines (Rubin et al. 1998). The FIR method has, however, been found to be more reliable because the lines are less affected than the optical lines by the so-called "geometry effect" (Rubin et al. 1988). Following their procedure, we derived N/O under the hypothesis that the volume occupied by N$^{++}$, $V$(N$^{++}$) is equal to $V$(O$^{++}$) (this is reasonably true if T$_{\rm eff} \leq$ 40000 K, R94), and the electron density and temperature remain constant over this volume. In this case

$$\frac{N}{O} = \frac{N^{++}}{O^{++}} = \frac{F_{57}/j_{57}}{F_{52}/j_{52}} = 0.4 \pm 0.1 \quad (2)$$

The j$_{57}$/j$_{52}$ ratio has been adopted from Lester et al. (1987). The value obtained is in agreement with the determinations derived with FIR methods in other HII Galactic regions, and in particular, for regions far from the Galactic centre, i.e. with R$_G \geq$ 7 kpc (Rubin et al. 1988).

## 5. Conclusions

The main conclusions from this work can be summarised as follows:

- ISO-LWS observations of the NGC 2024 star forming region, toward the two Class 0 sources FIR3 and FIR5 and the infrared source IRS2, find high-$J$ CO lines (from $J_{\rm up}$=17 to $J_{\rm up}$=14), together with the fine structure lines of [O I], [C II], [N II], [N III], [O III].
- The relative uniformity of the line intensities in all the pointed positions suggests that these lines are emitted from the whole cloud and not from the local enviroment around each source.

**Table 7.** CLOUDY results.

| Line ($\mu$m) | Log ($L_{obs}$) | Log ($L_{mod}$) |
|---|---|---|
| *IRS2* | | |
| [O III] 51.87 | 33.72 | 33.71 |
| [N III] 57.36 | 33.26 | 33.66 |
| [O I] 63.22 | 34.35 | 33.80 |
| [O III] 88.36 | 33.26 | 33.26 |
| [N II] 121.90 | 33.05 | 32.94 |
| [O I] 145.58 | 33.64 | 31.72 |
| [C II] 157.72 | 33.95 | 32.98 |
| *FIR3* | | |
| [O III] 51.87 | 33.48 | 33.43 |
| [N III] 57.36 | 32.99 | 33.43 |
| [O I] 63.22 | 34.23 | 32.69 |
| [O III] 88.36 | 33.08 | 32.99 |
| [N II] 121.90 | 32.86 | 32.72 |
| [O I] 145.58 | 33.55 | 31.61 |
| [C II] 157.72 | 33.77 | 32.75 |
| *FIR5* | | |
| [O III] 51.87 | 33.08 | 32.81 |
| [N III] 57.36 | $<$33.17 | 33.14 |
| [O I] 63.22 | 34.26 | 32.57 |
| [O III] 88.36 | 33.08 | 32.89 |
| [N II] 121.90 | $<$32.84 | 32.86 |
| [O I] 145.58 | 33.53 | 31.56 |
| [C II] 157.72 | 33.68 | 33.18 |

*Note:* Luminosities are expressed in erg s$^{-1}$.

– The molecular data have been consistently fitted with an LVG model. The emission originates in a diffuse, dense ($n_{\rm H_2} \sim 10^6$ cm$^{-3}$) and warm gas ($T\sim$ 100 K). CO column densities greater than $10^{18}$ cm$^{-2}$ are derived over the whole region.
– The I([O I]63)/I([O I]145) intensity ratio is definitely lower than that predicted by current PDR models, but can be explained if both lines are optically thick and have about the same temperature of CO. Alternatively, and more likely in our opinion, the ratio can be explained by strong absorption of the [O I] 63 $\mu$m line from the foreground cold gas along the line of sight. In this case the [O I] lines come from the warmer PDR gas ($T \gtrsim 500$ K), a scenario which has been identified also as responsible for the bulk of the [C II] 158 $\mu$m line emission.
– Clumpy PDRs appear to be by far the dominant source of both the atomic and molecular emission. The derived FUV radiation intensity is fully consistent with that produced by the OB star cluster present in the region if the molecular core is located nearby the interface with the ionised gas.
– The ionised emission has been succesfully modelled with CLOUDY, with the resulting model that the observed luminosities are produced by an equivalent O9.5 ZAMS star which also can account for the ionising capability of the cluster.
– From the intensity ratios of the ionic lines the electron density throughout the HII region and a N/O abundance of 0.4 are derived. This latter is in agreement with other determinations obtained via FIR methods in other HII regions far from the Galactic centre.

*Acknowledgements.* We would express our thanks to the anonymous referee whose helpful comments and suggestions have greatly contributed to improve the paper. We are also grateful to S.J. Leeks for her careful reading of the manuscript.

## References

Anthony-Twarog B.J. 1982, AJ 87, 1213
Barnes P.J., Crutcher R.M., Bieging J.H., Storey J.W.V., Willner S.P. 1989, ApJ 342, 883 (B89)
Benedettini M., Nisini B., Giannini T. et al. 2000, A&A in press
Burton M.G., Hollenbach D.J., Tielens A.G.G.M. 1990, ApJ 365, 620
Chackerian C., Tipping R.H. 1983, J. of Molecular Spectroscopy 99, 431
Chandler C.J., Carlstrom J.E. 1996, ApJ 466, 338
Clegg P.E., Ade P.A.R., Armand C. et al. 1996, A&A 315, L38
Crutcher R.M., Henkel,C., Wilson T.L., Johnston K.J., Bieging J.H. 1986, ApJ 307, 302
Crutcher R.M., Roberts D.A., Troland T.H., Goss W.M. 1999, ApJ 515, 275
Draine B.T., Roberge W.G., Dalgarno A. 1983, ApJ 264, 485
Ferland G.J. 1996, *Hazy, a Brief Introduction to Cloudy*, University of Kentucky, Department of Physics and Astronomy Internal Report
Flower D.R., Launay, J.M. 1985, MNRAS 214, 271
Giannini T., Lorenzetti D., Tommasi E. et al. 1999, A&A 346, 617
Graf U.U., Genzel, R., Harris A.I. et al. 1990, ApJ 358, L49 (G90)
Graf U.U., Eckart A., Genzel R. et al. 1993, ApJ 405, 249 (G93)
Habing H.J. 1968, Bull. Astr. Inst. Netherlands 19, 421
Harris A.I., Stutzki J., Genzel R. et al. 1987, ApJ 322, L49
Heiles C. 1994, ApJ 436, 720
Hollenbach D., Mc Kee C.F. 1989, ApJ 342, 306
Hollenbach D.J., Tielens A.G.G.M. 1997, ARAA 35, 179
Jaffe D.T., Genzel R., Harris R. et al. 1990, ApJ 353, 193
Jaffe D.T., Zhou S., Howe J.E., Stacey G.J. 1994, ApJ 436, 203
Jiang D.R., Perrier C., Lena P. 1984, A&A 135, 249
Kaufman M.J., Wolfire M.G., Hollenbach D.J., Luhman M.L. 1999, ApJ 527, 813
Kessler M.F., Steinz J.A., Anderegg M.E. et al. 1996, A&A 315, L27
Kraemer K.E., Jackson J.M., Lane A.P. 1998, ApJ 503, 785
Lester D.F., Dinerstein H.L., Werner M.W. et al. 1987, ApJ 320, 573
Lorenzetti D., Tommasi E., Giannini T. et al. 1999, A&A 346, 604
Luhman M.L., Jaffe D.T., Sternberg A., Herrmann F., Poglitsch A. 1997, ApJ 482, 298
Mangum J.G., Wootten A., Barsony M. 1999, ApJ 526, 845
Meyer D.M., Jura M., Cardelli J.A. 1998, ApJ 493, 222
Mezger P.G., Chini R., Kreysa E., Wink J.E., Salter C.J. 1988, A&A 191, 44
Mezger P.G., Sievers A. W., Haslam C.G.T. et al. 1992, A&A 256, 631
Moore T.J.T., Chandler C.J., Gear W.K., Mountain C.M. 1989, MNRAS 237, 1P
Mundy L.G., Evans N.J.II, Snell R.L., Goldsmith P.F. 1987, ApJ 318, 392
Nisini B., Benedettini M., Giannini T. et al. 1999, A&A 350, 529
Nisini B., Smith H.A., Fischer J., Geballe T.R. 1994, A&A 290, 463
Petuchowski S.J., Bennett C.L. 1993, ApJ 405, 591

Poglitsch A., Herrmann F., Genzel R. et al. 1996, ApJ 462, L43
Richer J.S. 1990, MNRAS 245, 24P
Richer J.S., Hills R.E., Padman R. 1992, MNRAS 254, 525
Rubin R.H., Martin P.G., Dufour R.J., et al. 1998, ApJ 495, 891
Rubin R.H., Simpson J.P., Erickson E.F. et al. 1988, ApJ 327, 377
Rubin R.H., Simpson J.P., Lord S.T. et al. 1994, ApJ 420, 772 (R94)
Sanders D.B., Willner S.P. 1985, ApJ Letters 293, L39
Saraceno P., Nisini B., Benedettini M. et al. 1998, Proc. of Star Formation with the Infrared Space Observatory, ASP Conf. Series vol.132, Eds. J.L. Yun, R. Liseau, p.233
Schultz A., Güsten R., Zylka R., Serabyn E. 1991, A&A 246, 570
Snell R.L., Mundy L.G., Goldsmith P.F., Evans N.J.II, Erikson N.R. 1984, ApJ 276, 625
Stutzki J., Stacey G.J., Genzel R. et al. 1988, ApJ 332, 379
Swinyard B.M., Clegg P.E., Ade P.A.R. et al. 1996, A&A 315, L43
Thompson R.I., Thronson H.A.Jr, Campbell B.G. 1981, ApJ 249, 622
Thronson H.A.Jr., Lada C.J., Schwartz P.R. et al. 1984, ApJ 280, 154
Tielens A.G.G.M., Hollenbach D. 1985, ApJ 291, 722
Visser A.E., Richer J.S., Chandler C.J., Padman R. 1998, MNRAS 301, 585
Wright C.M., van Dishoeck E., Cox P., Sidher S.D., Kessler M.F. 1999, ApJ 515, L29